

Internal Solitary Waves within the Cold Tongue of the Equatorial Pacific Generated by Buoyant Gravity Currents

A. M. SANTOS-FERREIRA,^{a,b} J. C. B. DA SILVA,^{a,c} B. ST-DENIS,^d D. BOURGAULT,^d AND L. R. M. MAAS^{b,e}

^a Department of Geosciences Environment and Spatial Planning, Faculty of Sciences, University of Porto, Porto, Portugal

^b Interdisciplinary Centre of Marine and Environmental Research (CIIMAR), Porto, Portugal

^c Institute of Earth Sciences (ICT), Porto, Portugal

^d Institut des sciences de la mer de Rimouski, Université du Québec à Rimouski, Rimouski, Quebec, Canada

^e Institute for Marine and Atmospheric Research Utrecht, Utrecht University, Utrecht, Netherlands

(Manuscript received 4 August 2022, in final form 26 July 2023, accepted 31 July 2023)

ABSTRACT: The equatorial cold tongue in the Pacific Ocean has been intensely studied during the last decades as it plays an important role in air–sea interactions and climate issues. Recently, Warner et al. revealed gravity currents apparently originating in tropical instability waves. Both phenomena have strong dissipation rates and were considered to play a significant role in cascading energy from the mesoscale to smaller horizontal scales, as well as to vertical scales less than 1 m. Here, we present Sentinel-3 satellite observations of internal solitary waves (ISWs) in the Pacific cold tongue near the equator, in a zonal band stretching from 210° to 265°E, away from any steep bottom topography. Within this band these waves propagate in multiple directions. Some of the waves' characteristics, such as the distance between wave crests, crest lengths, and time scales, are estimated from satellite observations. In total we identify 116 ISW trains during one full year (2020), with typical distances between crests of 1500 m and crest lengths of hundreds of kilometers. These ISW trains appear to be generated by buoyant gravity currents having sharp fronts detectable in thermal infrared satellite images. A 2D numerical model confirms that resonantly generated nonlinear internal waves with amplitudes of $O(10)$ m may be continuously initiated at the fronts of advancing gravity currents.

SIGNIFICANCE STATEMENT: Satellite imagery reveals the repeated occurrence of internal solitary waves in the near-equatorial region of the east Pacific, despite the absence of topography. These waves appear to be resonantly generated over the sheared Equatorial Undercurrent by gravity currents that propagate as frontal zones of 1000-km scale tropical instability waves, providing a physical link with viscous mixing scales.

KEYWORDS: Pacific Ocean; Internal waves; Solitary waves; Density currents; Remote sensing; Numerical analysis/modeling


1. Introduction

Intense ocean fronts along the eastern equatorial Pacific, observed in a zonal band from 5°S to 5°N, have been frequently reported in literature. For example, Warner et al. (2018, hereafter WEA) presented observations and model simulations of two major fronts in this region, the North and South Equatorial Fronts (NEF and SEF, respectively) that bound the equatorial cold tongue (Fig. 1). These fronts are frequently populated with eddies that develop into tropical instability waves (TIWs) possessing sharp gradients in surface temperature, surface salinity, and ocean color. They can be observed in satellite sea surface temperature (SST) images, especially during La Niña years, as will be presented below.

During La Niña and ENSO-neutral years, TIWs with wavelengths of about 1000 km are present during the boreal autumn and winter, owing to the intensification of the trade winds that shape the upper equatorial circulation (Willett et al.

2006) into westward-flowing North and South Equatorial Currents (NEC, SEC) in between which lies the eastward-flowing North Equatorial Counter Current (NECC). Beneath the SEC, the subsurface Equatorial Undercurrent (EUC) flows eastward, with a core centered at about 100 m at 220°E that shoals from west to east. The upper currents (especially the NEC and NECC) may become unstable owing to strong horizontal shear between the westward-flowing NEC and SEC and the eastward-flowing NECC and EUC, molding the NEF into a wave-like pattern of cold crests (or cusps) and warm troughs, usually confined southward of 5°N down to the equator. Typical TIW periods peak at 17 and 33 days (Lyman et al. 2007; Willett et al. 2006). The sharpening of the NEF and SEF is well documented, e.g., in thermal imagery from satellites (WEA; Caltabiano et al. 2005), but not much is known about the physical processes involved in their intensification in late boreal summer and autumn, or about their subsequent dissipation, typically at the end of boreal winter.

Associated with TIWs are coherent anticyclonic tropical instability vortices (TIVs) that slowly propagate westward at quasi-steady phase velocities, dissipating in the western Pacific after a couple of months (Fig. 1). While TIVs are highly coherent throughout their lifespan, they can exchange up to 50% of their water mass with the surroundings

 Denotes content that is immediately available upon publication as open access.

Corresponding author: Leo R. M. Maas, l.r.m.maas@uu.nl

DOI: 10.1175/JPO-D-22-0165.1

© 2023 American Meteorological Society. This published article is licensed under the terms of the default AMS reuse license. For information regarding reuse of this content and general copyright information, consult the AMS Copyright Policy (www.ametsoc.org/PUBSReuseLicenses).

were visible from ships, aircrafts, and satellites, as being “remarkably straight and narrow.” Johnson (1996) also encountered a sharp front at 2.1°N, 220°E along the western (leading) edge of a TIW cold cusp that exhibited downward velocities close to 1 cm s^{-1} and a horizontal momentum balance between pressure gradient force and advection. This front was interpreted as part of a propagating gravity current made of warm water overriding the colder water (i.e., equatorial cold tongue), consistent with a nonrotating gravity-flow theory of subducting dissipative fronts (Johnson 1996). It has been suggested that some of the front’s energy loss was through turbulent dissipation, similarly to the SSFs reported by WEA, but a considerable portion must have gone through some other mechanisms, possibly in the form of radiating interfacial internal waves (Johnson 1996). However, the theory used by Johnson (1996) was inadequate to test this hypothesis. The main goal of the present study is to examine the possibility that small-scale fronts could radiate internal wave energy in the equatorial Pacific.

2. Data and methods

We use combined satellite image data, in situ data and numerical modeling to investigate the characteristics and origin of ISWs in the zonal band of the equatorial Pacific Ocean (from 5°S to 5°N) that are mostly visible inside the surface cold tongue. Combining SST satellite images with visible images affected by sun glint allows for the observation of both ocean fronts and ISW surface manifestations owing to gradients in surface roughness. Currents within the ISWs are characterized by convergent and divergent flow at the sea surface propagating in phase with the internal wave’s subsurface waveform at the main pycnocline. These convergence/divergence surface bands cause variations in sea surface roughness at meter and submeter spatial scales that appear as distinctive bright features in optical sun glint imagery (Santos-Ferreira et al. 2022). A high-resolution nonlinear and nonhydrostatic numerical model is used to complement satellite observations and estimate some ISW characteristics not retrievable from satellite data. The model also provides insights into the mechanisms of wave generation.

a. Satellite data

Our observation method consists of visual recognition of ISWs in Level-1b Ocean and Land Color Instrument (OLCI) optical imagery from top-of-atmosphere (TOA) radiometric measurements provided by the European Space Agency’s (ESA) Copernicus Open Access Hub. These images are geometrically corrected, calibrated, and provided as optical multi-channel band images. The images are also ortho-geolocated, with geographic coordinates provided for each image pixel with a nominal spatial resolution of 300 m at nadir. This optical sensor on board of *Sentinel-3A* and *Sentinel-3B* satellites provides quasi-true color images over a swath width of 1270 km, covering most of the equatorial Pacific on a daily basis. The OLCI swath is not centered at nadir in order to mitigate the effects of sun glint patterns (direct specular reflection of the Sun in the ocean) but has a westward inclination. However, these

sun glint patterns allow easier visibility of oceanic internal waves.

We use Sea and Land Surface Temperature Radiometer (SLSTR) products from Sentinel-3 satellites, namely, the Level-2 Water Surface Temperature (WST) product providing SST. The spatial resolution of the SLSTR is 1 km, covering a swath width of 1400 km, and the sensing data are obtained simultaneously, i.e., synergistically, with an accuracy of 0.2 K, because these instruments (OLCI and SLSTR) are on the same platform.

The SEF and NEF have a surface thermal signature, visible only when cloud coverage is reduced. Obviously, cloud cover is very frequent around the equator, where cloudiness over the ocean is around 72% (King et al. 2013). Hence, we complement the SLSTR observations with the Multi-Scale Ultra High Resolution (MUR) SST image data available daily from NASA JPL Physical Oceanography DAAC (<https://doi.org/10.5067/GHM25-4FJ42>). MUR imagery is a global, gap-free, gridded, daily SST dataset created by merging multiple Level-2 satellite SST datasets. Data are available from 2002 to present (Chin et al. 2017).

A satellite image dataset has been assembled with images showing fronts and ISWs for the year 2020 during which a moderate to strong La Niña event emerged. The statistical analysis (section 3d) is conducted on data between 230° and 265°E, and between 5°S and 5°N. For 2020, 19 relative orbits of *Sentinel-3A* and 19 relative orbits of *Sentinel-3B* are chosen for scrutiny. These 38 orbits correspond to, respectively, 12 and 13 satellite cycles (an orbit cycle is the time taken for the satellite to pass over the same geographic point, being 27 days for *Sentinel-3A* and *Sentinel-3B*). Sharp fronts and ISWs are more commonly observed between April and August, as a result of greater cloud cover during other periods of the year. The ISWs that are visible (with distinguishable amplitude and large enough crest-to-crest distance—for short, hereafter referred to as ISW “wavelength”) are consistent with a generation by oceanic fronts. By “consistency,” we mean crest orientations nearly parallel to the oceanic fronts visible in the same image and within reasonable distances from these fronts (typically on the order of 10–100 km, but sometimes much larger distances).

The phase speed of the ISWs is estimated from satellite data. For this, images on consecutive days are geolocated in the same projection and with the same resolution, overlapping them side by side. In these images, the ISWs leading crests are determined. Their average distance was calculated assuming a set of seven representative points along the first image. We determine the minimum distance of each of these points to points on the wave front on the following day. Since we know the exact times of the satellite images’ acquisition, a reasonable estimate of the propagation speed of the ISW train is obtained by dividing the average distance between the two sets of points by the elapsed time. This method provides good results in previous studies (see, e.g., da Silva et al. 2011; Tensubam et al. 2021), as long as wave fronts do not change shape significantly in the time elapsed between the images.

TABLE 1. Parameter values for each model run. Densities ρ are given in kg m^{-3} ; velocities u in m s^{-1} ; and depth scales h , d , and L in m.

Run	ρ_0	ρ_1	ρ_2	u_{01}	u_{02}	u_1	u_2	h_1	h_2	d_1	d_2	L
1	1026.5	1023.5	1023.3	0.5	0.502	-0.14	-0.36	40	40	15	10	50
2	1026.5	1023.5	1023.3	0.5	0.506	-0.14	-0.36	100	100	15	10	50

b. *In situ data*

To characterize density stratification in the ocean, we use monthly mean climatological data provided by NOAA/OAR/ESRL PSD, Boulder, Colorado, available online at <https://www.cpc.ncep.noaa.gov/products/GODAS/>. The dataset has a global spatial coverage, with resolution of 0.333° in latitude and 1.0° in longitude, and 40 vertical levels from 5- to 4478-m depth. Climatological stratification profiles are used to compute the linear phase speed of internal waves propagating in the study region under the influence of climatological shear currents, such as the EUC (Behringer and Xue 2004). A MATLAB code provided by Oregon State University tools in <https://blogs.oregonstate.edu/salty/matlab-tools-to-solve-the-viscous-taylor-goldstein-equation-for-both-instabilities-and-waves/> is used to solve the inviscid Taylor–Goldstein equation, providing theoretical estimates of the linear internal wave phase speed (Miles 1961; Smyth et al. 2011; Lian et al. 2020).

c. *Numerical modeling*

Numerical simulations are performed to examine whether a gravity current with the hydrographic conditions typical of the study region reported by WEA (0° , 220°E and 0.75°N , 250°E) would be capable of generating ISWs. We use the nonhydrostatic and nonlinear 2D model of Bourgault and Kelley (2004) that solves the nonrotating Euler equations in a vertical (x - z) plane. This model has previously been used in a similar configuration to simulate ISWs arising from gravity currents, but

in different regions than WEA (Bourgault et al. 2016; Mendes et al. 2021).

The model domain is a two-dimensional ocean that extends laterally over a distance of 2000 km and vertically over a depth of 4360 m, representative of the mean depth in the region (Smith and Sandwell 1997). The model domain is bounded by a free surface, the ocean bottom, and open boundaries at $x = \pm 1000$ km. The Arakawa-C grid has 2296 points horizontally and 214 points vertically. The horizontal resolution decreases with distance from the central part of the domain ($-10 \text{ km} < x < 10 \text{ km}$). The smallest horizontal grid spacing (near the center of the domain) is $\Delta x = 10$ m. This resolution exponentially decreases to $\Delta x = \pm 10$ km toward the open boundaries. The open boundaries are located far away (± 1000 km) from the region of interest to minimize the influence of open boundary conditions. At the open boundary, far away from the central region of interest, Neumann conditions are taken, such that during the computation time (1 h) any waves reflecting from these boundaries have not yet returned to this region. The vertical grid spacing is $\Delta z = 1$ m in the upper 150 m and progressively decreases to $\Delta z = 370$ m at the bottom. The duration of the model integration is 1 h and the model output is every 5 s for all variables analyzed in this manuscript.

The model is initialized with a density field that mimics the gravity current observed by WEA. The initial density field is separated in three water masses with different densities: two surface layers (ρ_1 , ρ_2) are separated by a front of width (L)

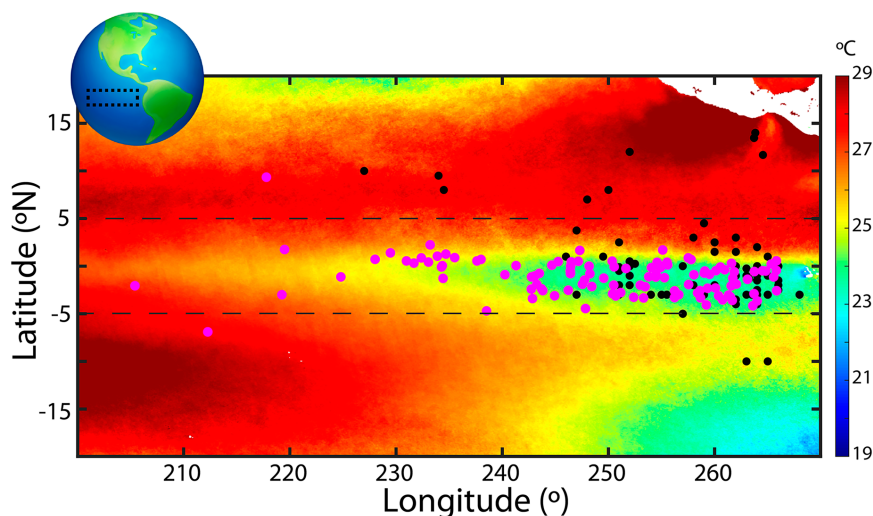


FIG. 2. Spatial distribution of the ISWs found in this study (magenta dots) for the year 2020. The black dots are the ISWs reported in Jackson et al. (2012). A MUR SST annual average image for the year 2020 is shown in the background.

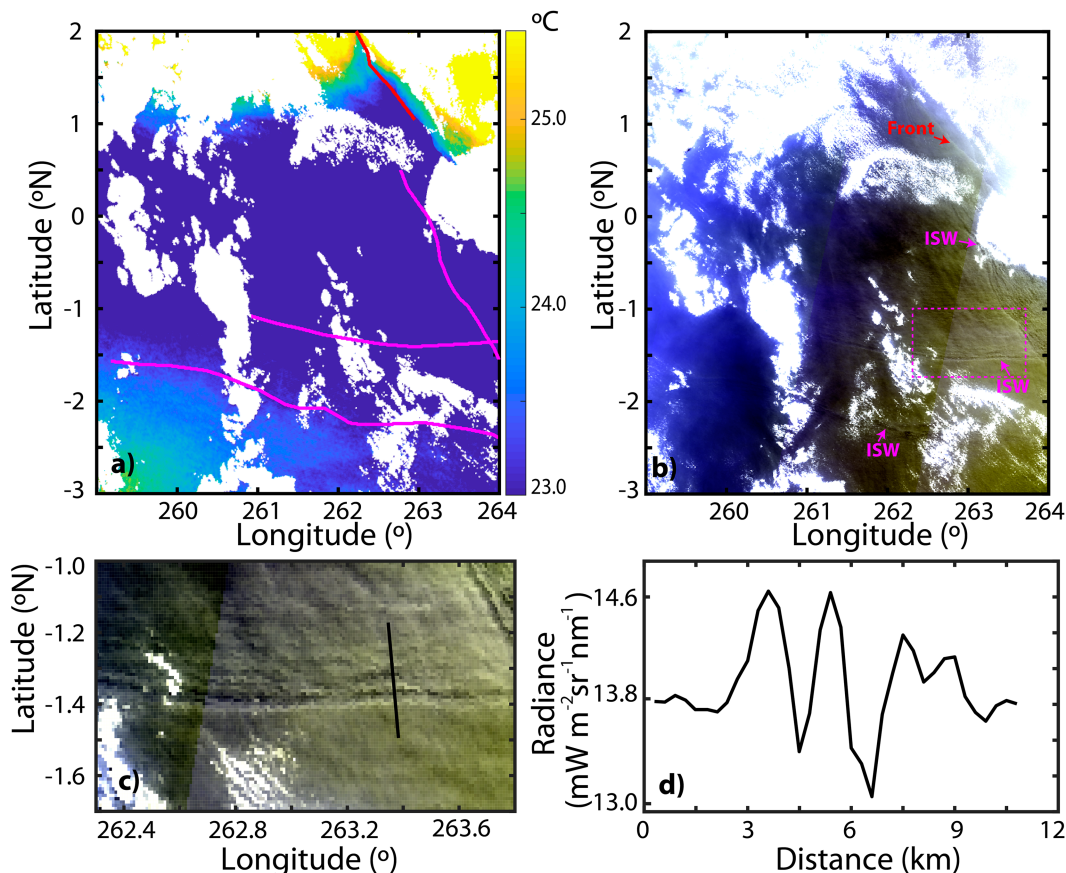


FIG. 3. (a) *Sentinel-3B* thermal infrared image (Level 2 WST) dated 7 Jun 2020, acquired at 1516:19 UTC (start time). The magenta lines and the red line are contours of the ISWs leading crests and the ocean front, respectively, also identified in (b). (b) *Sentinel-3B* visible image (Level 1b OLCI) simultaneous with (a) and presented in quasi-true color. The magenta arrows indicate the ISWs, and the red arrow indicates the front. (c) Zoom of image section (magenta rectangle) in (b) over 1.7° – 1° S and 262.3° – 263.8° E showing surface manifestations of ISWs owing to sun glint. The black line, perpendicular to the ISW crests indicates an image transect, shown in (d). (d) Radiance image transect (red band, 665 nm). The distance along the horizontal axis increases from south to north.

centered at $x = 0$ m overlying a denser bottom layer (ρ_0) (Fig. 1c). The surface layers are separated from the bottom layer by a pycnocline of half-thickness d_1 , d_2 centered at a depth of h_1 , h_2 , respectively. The vertical density distribution within the pycnocline follows a hyperbolic tangent shape where ρ_i , d_i , h_i , ($i = 1, 2$) and ρ_0 determine its steepness. The same function is used to create the front, except that L , instead of d_i , determines the horizontal gradient of horizontal velocities and densities. Two model simulations are set up to represent idealizations of the observations made by WEA (see parameters in Table 1). In section 3e, Run 2 will be taken as reference, as it is the simulation that best fits the gravity current average depth, hence best fits the observations on 2 November 2008 (WEA).

The velocity field at time $t = 0$ is defined in a similar manner to the density field described above. There are two surface velocities u_1 , u_2 , respectively associated with the surface layers of density ρ_1 , ρ_2 , and the horizontal velocity distribution across the front follows a hyperbolic tangent function with u_i ,

L , x as parameters. However, the velocity field of the deeper (ρ_0) layer comprises two components u_{01} , u_{02} (see Table 1). The velocity field u_{01} occurs below the surface layer with density ρ_1 , which is on the left, southwestward side of the front. The velocity u_{02} , below the surface layer with density ρ_2 , is initially calculated to balance the transport on each side of the front. For more details about the model setup, the reader is referred to Bourgault and Kelley (2004) and Bourgault et al. (2016), and references therein.

3. Results

Satellite imagery in 2020 shows that in the eastern equatorial Pacific ISWs cluster around the equatorial waveguide (between 5° S and 5° N). This occurs preferentially within the cold tongue, where TIWs are most energetic (see Fig. 2). These ISWs are found in 103 Level-1b *Sentinel-3* OLCI images, selected by visual inspection of cloud-free images (for both *Sentinel-3A* and *Sentinel-3B* satellites). In each image, the

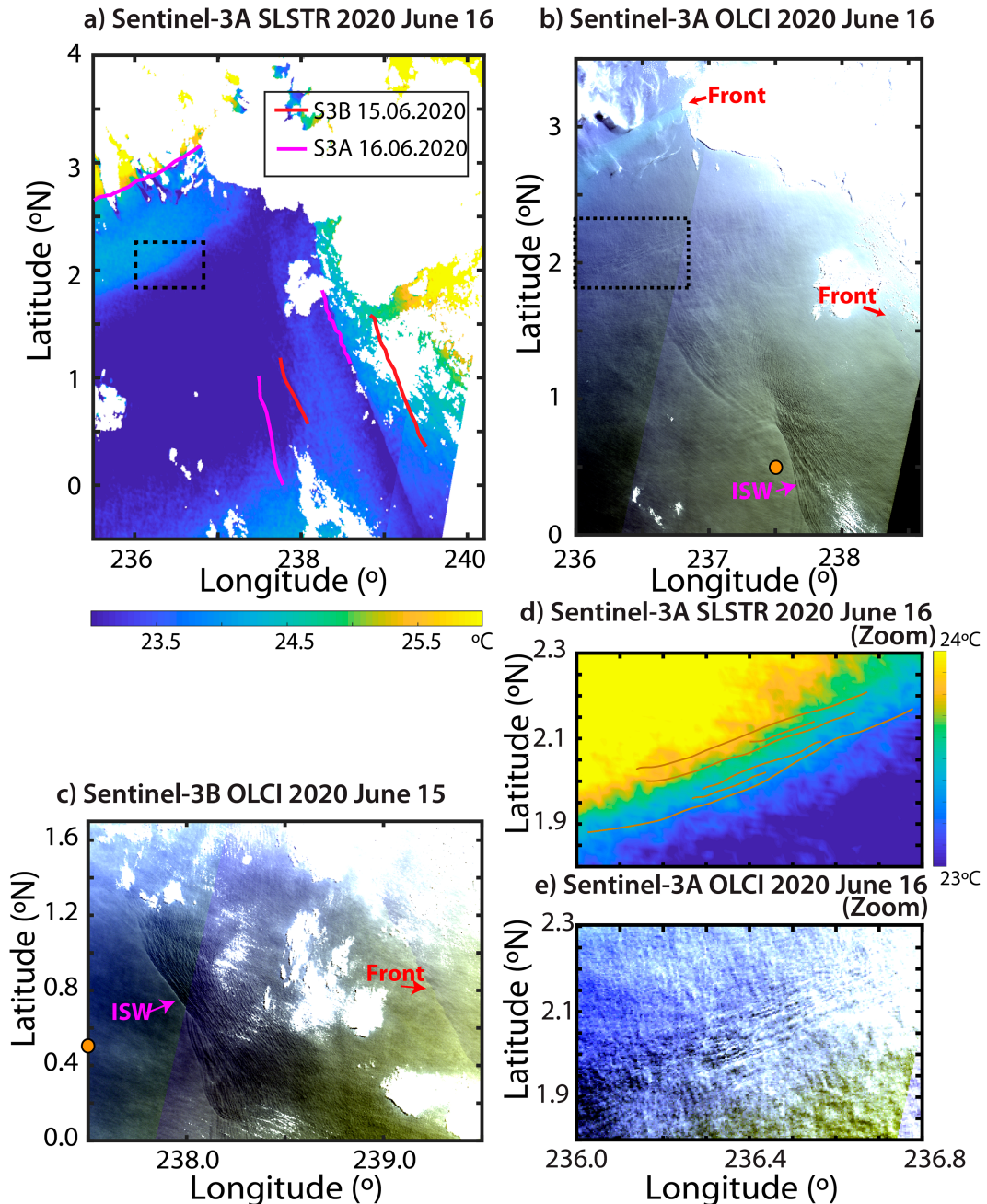


FIG. 4. (a) *Sentinel-3A* thermal infrared image (Level 2 WST) dated 16 Jun 2020, acquired at 1816:24 UTC (start time). The magenta and red lines are contours of the ISW leading crest and the ocean front identified in (b) and (c), respectively. The black rectangle corresponds to (d). (b) *Sentinel-3A* visible image (Level 1b OLCI) simultaneous with (a) and presented in quasi-true color. The magenta colored arrow indicates the ISWs, and the red arrows indicate the fronts that are visible in the image. The black rectangle corresponds to (e). (c) *Sentinel-3B* visible image (Level 1b OLCI) dated 15 Jun 2020, acquired at 1803:08 UTC (start time) and presented in quasi-true color [same label codes as in (a) and (b)]. (d) Zoom of image section indicated by black rectangle in (a), over 1.80° – 2.30° N and 236° – 236.8° E, showing the SST gradient across the front (color bars do not span the same range). The brown lines are manifestations of roughness that are seen in (b) and (e). (e) Zoom of image section indicated by black rectangle in (b) over 1.80° – 2.30° N and 236° – 236.8° E showing roughness linear features due to sun glint. The orange points in (b) and (c) correspond to the location of climatology data used in section 3c.

centers of the largest ISWs are selected, marked in Fig. 2 (magenta dots). In 13 images we find two or more centers for different ISW trains. Each “center” is defined as the middle of the crest of the first soliton of each ISW train. The same map shows ISWs (black dots) registered in Jackson et al. (2012) using the method described in section 2 (see also Fig. 1a and Jackson 2007). These authors made a global map of ISWs, based on a comprehensive set of Moderate Resolution Imaging Spectroradiometer (MODIS) images, where they could identify the oceanic ISWs during a period of time greater than one year (from August 2002 until May 2004, corresponding to a mild El Niño period). However, we stress that no generation mechanism was attributed by these authors to the ISWs along the equatorial Pacific band.

a. Case studies

Two case studies provide insight into the generation mechanism of ISWs and allow us to estimate their average phase speed for particular days. In case 1, multiple fronts and ISWs are identified propagating in different directions, the common factor being that ISWs and thermal fronts are aligned in a quasi-parallel direction. This suggests a link between the thermal fronts and the generation of ISWs. In case 2, an estimation of the average propagation speed of ISWs (admittedly also linked to the thermal fronts) is made, based on observations separated in time by approximately one day.

Fronts and ISW signatures are identified first in visible satellite images. All ocean fronts are confirmed in thermal imagery, while most ISWs do not have a thermal signature due to reduced spatial resolution of both SLSTR (1 km) and MUR.

1) CASE 1: 7 JUNE 2020

Oceanic fronts are ubiquitous in both SST and quasi-true color images along the equator in a zonal band from 5°S to 5°N. Figure 3a, from 7 June 2020, shows a SLSTR SST color-coded image where a vast region of cold water is surrounded by warmer water to the north and south. A front can be distinguished in the northeastern part of the region, oriented along the northwest–southeast direction (red line). It is similar to the SSFs documented by WEA. The SST varies by at least 1°C across the front and occurs within one pixel of the image, in somewhat less than 1 km (which is the resolution of the SLSTR). The same pattern (“front”) is observed and indicated in the quasi-true color OLCI image (Fig. 3b). In the same figure, internal wave features are identified and labeled “ISWs.” One of these ISW crests has a similar orientation as the thermal front.

Joint analysis of Figs. 3a and 3b (SLSTR and OLCI) facilitates interpretation of various other ISWs leading crests (magenta lines). One of these is amplified in the zoom shown in Fig. 3c, where several ISW crests are visible and rank ordered in both image brightness and wavelength. According to nonlinear wave theory, the rank ordered wavelengths of these wave fronts is an indication of the nonlinear character of the wave train. Hence, we refer to these waves as ISWs, as is common in literature (Magalhães et al. 2021). This nonlinearity is confirmed in the image transect taken across the wave fronts

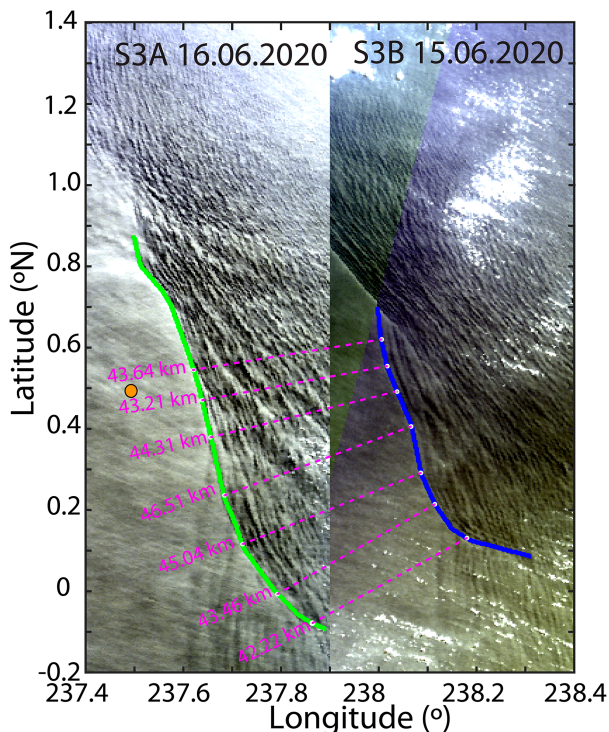


FIG. 5. Sentinel-3 visible images (Level 1b OLCI) (right) dated 15 Jun 2020 and (left) dated 16 Jun 2020. The leading ISWs are marked in blue and green, respectively. Magenta dashed lines mark distances between points on the same ISW leading crest, and are used to estimate the average wave propagation speed. Note that images are the same as in Figs. 4b and 4c. The two images are superposed on a georeferenced map. The orange dot gives the location of climatology data used in section 3c.

(black line in Fig. 3c), which is displayed in radiance levels along the wave profile (Fig. 3d). The first two waves exhibit larger radiance profiles and wavelengths, typical of nonlinear dispersive waves described in solitary wave-like theories (e.g., KdV theory, see Osborne and Burch 1980). In this example, the approximate wavelength of the first ISW is more than 1800 m.

2) CASE 2: 15–16 JUNE 2020

Figure 4a gives a synergistic view of fronts (red lines) and ISWs (magenta lines) found on 15 and 16 June 2020. These are shown in visible images in Figs. 4c and 4b, respectively, where the same ISW and front are visible. Figure 4a is a SLSTR SST color-coded image dated 16 June 2020 where a vast region of cold water is bounded by warmer water masses in the east and the northwest that are identified in Figs. 4b and 4c. Several fronts can be distinguished in the eastern half and in the northwest in Fig. 4a. The ISW leading crest in the eastern half (also visible in Fig. 3a) is oriented along the northwest–southeast direction, while the front in the northwest is oriented along the northeast–southwest direction. Both are similar to the SSFs documented by WEA, along the TEF and the LEF, respectively (Fig. 1). The same patterns

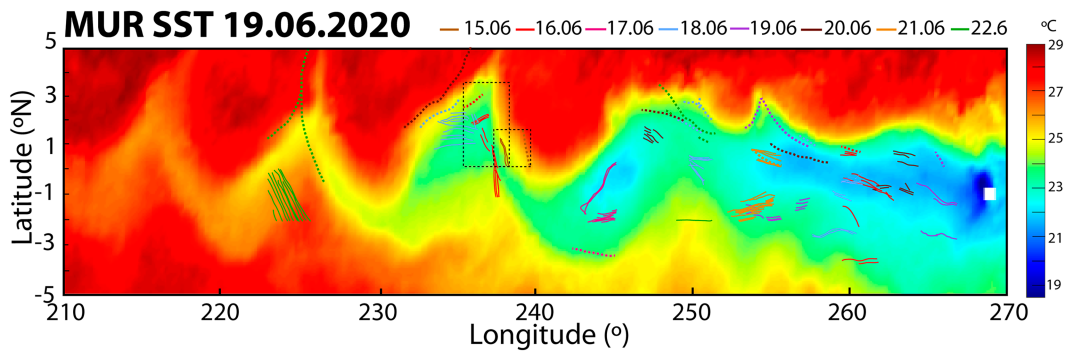


FIG. 6. Spatial distribution of the fronts (dotted lines) and ISW packets (solid lines), identified in the visible imagery of Sentinel-3, between 15 and 22 Jun 2020. The color for each day is identified in the upper part of the map. The dashed dark rectangles show the location of the images given in Figs. 4 and 5. A MUR SST image, dated 19 Jun 2020, is shown in the background.

are observed in the quasi-true color OLCI (Fig. 4b, acquired at the same time as Fig. 4a). A front and ISWs are also visible on 15 June 2020 (Fig. 4c). Figures 4d and 4e depict a zoom of Figs. 4a and 4b, respectively, over 1.80° – 2.30° N and 236° – 236.8° E (see dashed black rectangles in each figure). The thermal gradient in Fig. 4d coincides with small structure wavelike features in Fig. 4e. We will discuss these patterns and possible interpretations in section 4.

Geolocating and overlapping images from 15 to 16 June (Fig. 5) reveals the location of the ISW leading crest (blue and green lines, respectively), as well as a “corrugated pattern” to the east of these fronts. The latter are believed to represent internal waves in the wake of the leading ISW. Based on the average distance between these ISW crests and the elapsed time, the ISW phase speed is estimated to be $0.50 \pm 0.03 \text{ m s}^{-1}$.

b. Large-scale picture

Using Figs. 4 and 5 and other visible images which were partly cloud-free in the following 6 days, many ocean fronts and ISWs’ leading crests are identified and plotted onto a MUR SST composite image (Fig. 6). This mode of display gives insight into the zonal and lateral extent and frequency of occurrence of both ocean fronts and ISWs. Dotted and solid lines indicate (sharp) thermal fronts and ISWs, respectively, different colors representing different days. The MUR SST image in the background, from 19 June 2020, shows that the orientation of ISWs follow small-scale fronts, which in turn appear to follow those of the main TEF and LEF fronts referred to by WEA. Twelve visible images are used during 8 consecutive days, in the period 15–22 June 2020, extending along the equator over at least 45° in longitude. We identify 26 wave trains and 17 sharp fronts. Nine ISWs could be unambiguously associated with a specific front, leading to nine ISW–front pairs. The map in Fig. 6 is relevant because it is rare to find simultaneously ISWs and ocean fronts during several consecutive days owing to cloud coverage and sun glint. It is interesting to note the neat cusps and troughs of the TIWs delineating many of the sharp fronts (dotted lines), particularly to the north of the equator. Note, however, that the fronts that were found on 22 June 2020 are somewhat

displaced to the west in comparison to the MUR SST image. This is attributed to the time elapsed between the MUR SST image and the OLCI/SLSTR.

c. Prediction of internal wave linear phase speed in the study region

Climatological data are used to estimate the linear phase speeds for the internal waves described in sections 3a and 3b based on a standard boundary value problem (BVP) with appropriate boundary conditions of the form:

$$(U_i - c_i) \left(\frac{d^2}{dz^2} - k^2 \right) \varphi - \frac{d^2 U_i}{dz^2} \varphi + \frac{N^2}{U_i - c_i} \varphi = 0, \quad (1a)$$

$$\varphi(0) = \varphi(-H) = 0. \quad (1b)$$

In this Taylor–Goldstein equation (1a) (Miles 1961), $\varphi(z)$ represents the (vertical velocity) modal structure, z the vertical coordinate, H the local depth, and k the wavenumber. The phase speed c_i and horizontal currents $U_i(z)$ are given in east ($i = 1$) or north ($i = 2$) direction. Vertical profiles of Brunt–Väisälä frequency $N(z)$ and currents $U_i(z)$ are determined from climatology (Behringer and Xue 2004) at locations where the waves are observed (Fig. 6). However, note that those climatology profiles are long term averages, and particular vertical profiles may significantly exceed these.

For the case study exhibited in section 3a, Eq. (1a), subject to boundary conditions (1b), yields an estimate $c_1 = -0.5 \text{ m s}^{-1}$ for waves propagating to the west. This value agrees with the estimate obtained from the satellite images in section 3a, case 2 (using a wavelength of 600 m, considering the examples in that subsection). Figure 7 displays the vertical profiles of $N(z)$ and eastward directed $U_1(z)$ used in this calculation at 237.5° E and 0.5° N. The U_1 profile clearly shows easterly currents centered at about 100 m deep, which could interact significantly with the wave at that latitude. This current is the well-known EUC, a narrow 400-km-wide and fast undercurrent reaching speeds up to 1.5 m s^{-1} (Stellema et al. 2022). Disregarding these shear currents, the BVP yields a phase speed of about $\pm 0.76 \text{ m s}^{-1}$ (the \pm sign corresponding to eastward/westward wave propagation,

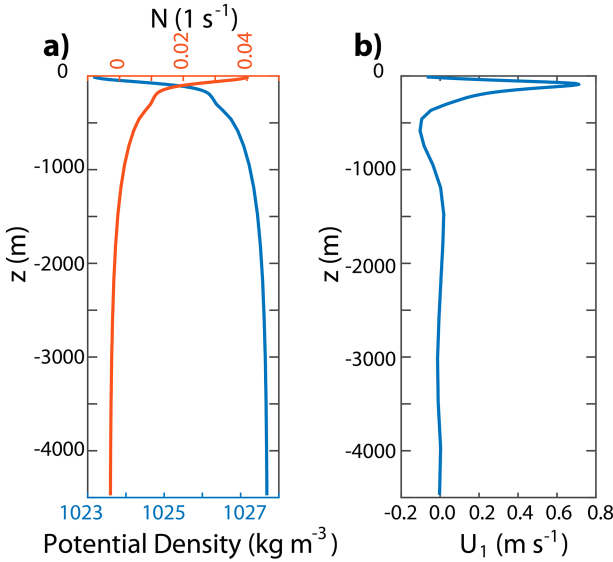


FIG. 7. (a) Potential density and buoyancy frequency (N) profiles in blue and orange colors, respectively. (b) U_1 velocity profile. All profiles are from monthly mean climatological data available at the location and time of the examples given in Figs. 4 and 5 (i.e., June 2020).

respectively). The eastward directed EUC reduces the westward propagating phase speed to -0.5 m s^{-1} in Earth’s reference frame, showing the importance of the background flow on wave speed.

The impact of the EUC is further illustrated in Fig. 8, where “west to east,” etc., refer to the internal wave propagation direction. Here, phase speeds, evaluated from Eqs. (1a) and (1b), are plotted between 5°S and 5°N along 237.5°E , where

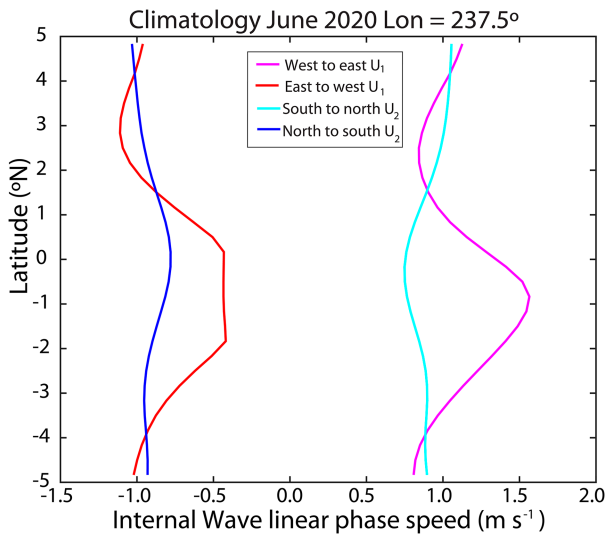


FIG. 8. Phase speeds of linear long internal waves evaluated for different vertical profiles of horizontal velocity (U_1 and U_2 , eastward and northward, respectively). The profiles of U_1 , U_2 , and density have been taken between 5°S and 5°N at the fixed longitude of 237.5°E .

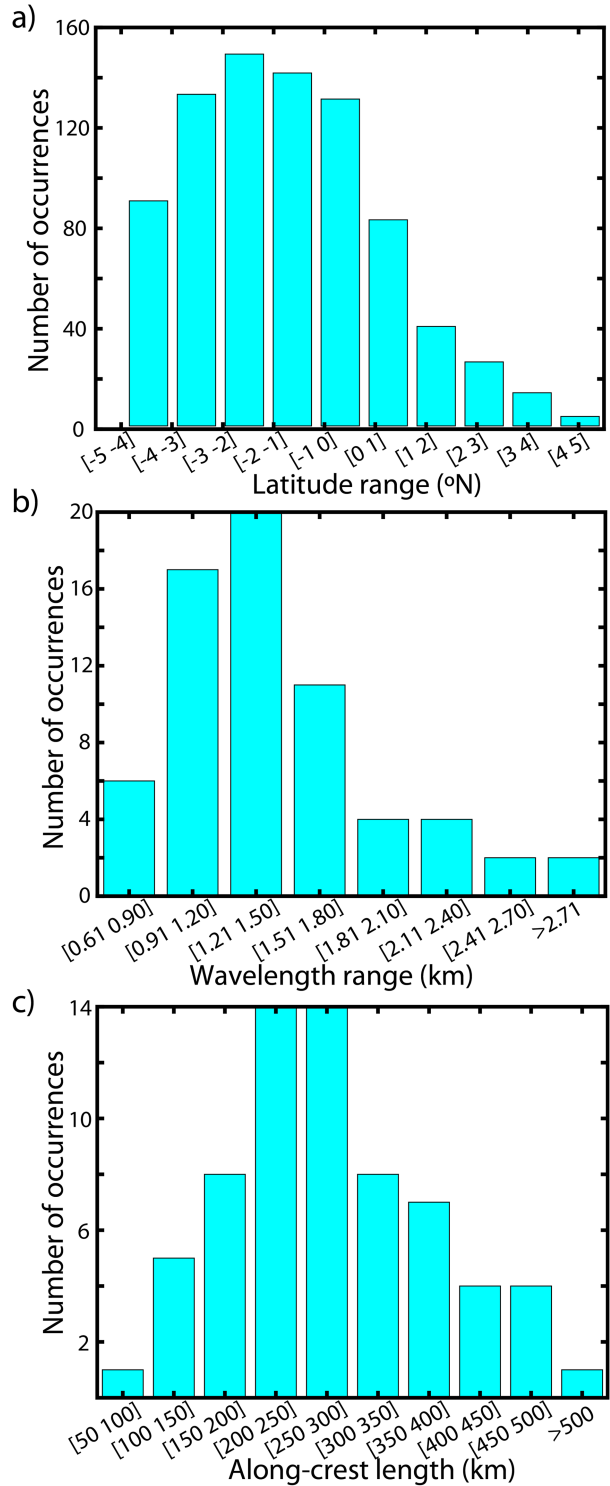


FIG. 9. (a) Latitude distribution of the 116 ISWs selected from 2020 images in the eastern equatorial Pacific Ocean. (b) Distribution of the ISW wavelengths for the best 66 cases for the same period of time. (c) As in (b), but for along-crest length scale.

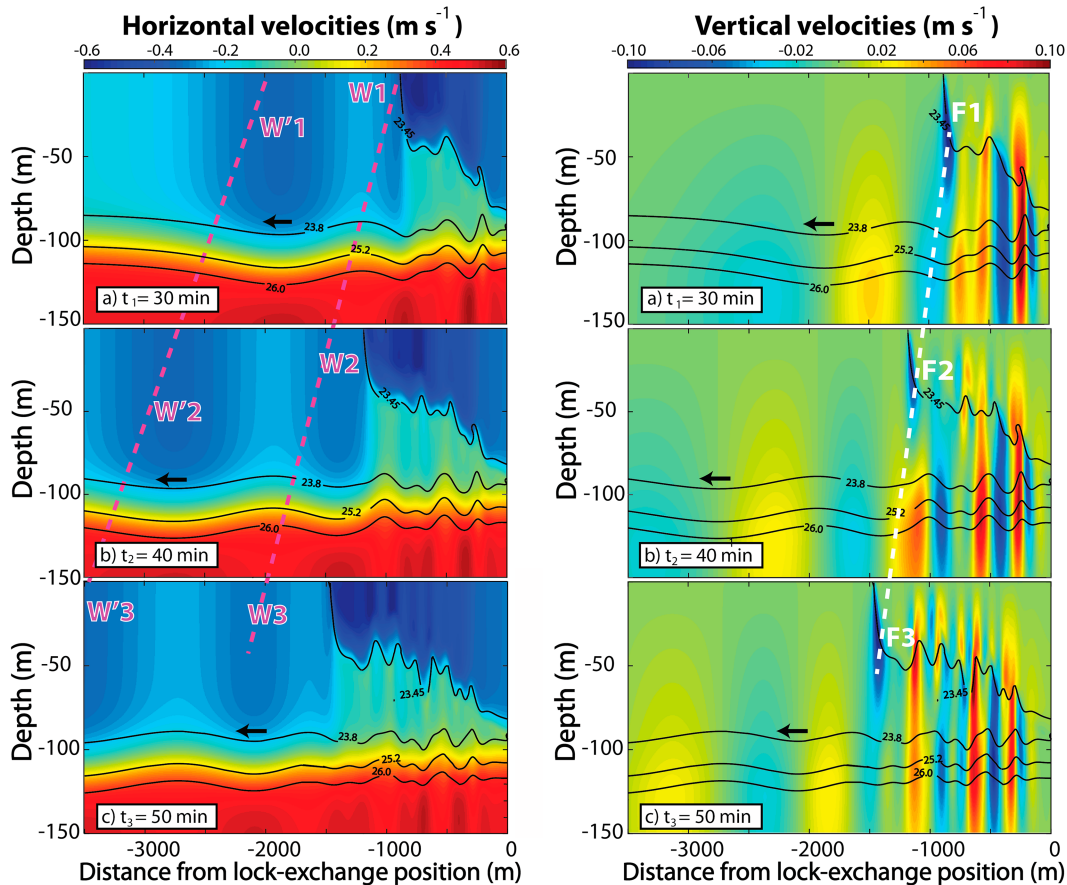


FIG. 10. Numerical simulations of ISWs generated by a gravity current at (a) $t = 30$ min, (b) $t = 40$ min, and (c) $t = 50$ min. In the six plots it is possible to see the ISW propagation from right to left. The colors represent the (left) horizontal velocities and (right) vertical velocities, while the black lines are density anomalies σ . The magenta dashed lines (left panels), namely, $W'1$, $W'2$, $W'3$, and $W1$, $W2$, and $W3$, are showing the propagation of consecutive ISWs. The white dashed lines (right panels) represent the propagation of the gravity current.

images reveal strong ISWs (Fig. 6). Due to shear in zonal currents, phase speed c_1 varies by as much as 67% for zonally propagating waves. Waves propagating in meridional direction are less affected by shear in meridional currents, with meridional phase speeds varying by 28% only. The main variation of the former occurs precisely where the EUC maximum is expected, between 2°S and 1°N (Behringer and Xue 2004). This “Doppler-like” effect is typical for internal waves propagating within strong quasi-steady ocean currents (see e.g., da Silva et al. 2011).

d. Statistics of wave observations

To determine the distance between subsequent crests and crest lengths we selected the “best” 66 cases of ISWs in the images. Here “best” relates to features that are most visible and/or largest, such that lengths can be measured with sufficient confidence. ISWs are most frequently observed from 5°S to 1°N (Fig. 9a). This may partly reflect the decrease in cloud cover inside this latitude band, and the occultation of ocean features by clouds outside this band. The most frequent ISW wavelength estimates in this sample are in the range between 900 and 1800 m, but waves with wavelengths larger than 4 km are also observed. Along-crest

lengths are frequently in the range between 200 and 300 km, as depicted in Fig. 9c. But ISW crests longer than 500 km are also found and are among the longest observed in the ocean (da Silva et al. 2011; Magalhães et al. 2016; Tensubam et al. 2021).

e. Model simulations

The initial conditions and parameter values used for the simulations are based on the observations of gravity currents shown by WEA. They involve fitting hyperbolic tangent functions to observational profiles of density and horizontal velocity. Two model runs are forced with different pycnocline depths, keeping other parameters approximately the same (Table 1). Here we present and discuss only one of the runs (Run 2) which reproduces reasonably well the measurements of November 2008, described by WEA; results from Run 1 are briefly mentioned but not displayed.

The initial conditions are intended to produce a gravitational adjustment to a lock-exchange configuration confined within the top 100 m (ambient surface layer, as sketched in Fig. 1c). The reason for this choice of upper layer thickness is

twofold: first, this is the typical depth of the main pycnocline in the study region, and second, it leads to buoyant gravity currents with thicknesses typically observed by WEA, particularly for the measurements of November 2008. This setting corresponds to Run 2 (see Table 1), when the model is adjusted to a three-layer setting. After gravitational adjustment the gravity current propagates at a constant speed, with an average thickness of 40 m.

Numerical model results (Fig. 10) show typical crest-to-trough amplitudes of 10 m and maximum horizontal and vertical velocities of approximately $u \approx -0.3 \text{ m s}^{-1}$ and $w \approx \pm 0.04 \text{ m s}^{-1}$. These results may be interpreted as ISWs that propagate to the west (left side in Fig. 10) into the equatorial cold tongue waters along the thermocline there, which is typically centered at 100-m depth. Furthermore, wavelengths of $\sim 1500 \text{ m}$ estimated from the model are consistent with the range of values measured in satellite images (Fig. 9b).

The velocity sections portrayed in Fig. 10 represent the essential phases in the ISW generation and evolution. The propagation of the gravity current (see labels F1, F2, and F3 and dashed white line), the waves' detachment from the front and evolution (labels W1, W2, and W3 and dashed magenta line), and the propagation of the ISWs as pycnocline depressions upstream of the front (labels W'1, W'2, and W'3 and dashed magenta line), are all identified in 20 min of model simulation. Using the maximum horizontal velocity at the surface as indicators of soliton centers, W' and W refer to two consecutive ISWs generated at the gravity current's front (labeled F). Indices 1, 2, and 3 stand for three different times of model output at 30, 40, and 50 min, respectively. The direction of wave propagation is indicated by horizontal black arrows. The wave amplitude and propagation speed increase through nonlinear dispersion. The wave is subsequently released from the front location when its phase speed significantly exceeds the front speed. If the front propagation is steady (for some period of time at least) the generation sequence is repeated after the complete detachment of the preceding solitary wave. In this process, energy is transferred from the gravity current to ISW trains.

A Hovmöller (space–time, time increasing downward) plot of the wave-induced horizontal velocity at the surface shows upstream-propagating ISWs, i.e., flowing in the opposite direction to the EUC (Fig. 11). These appear as red colored bands of negative velocity (well depicted by contour $u = -0.3 \text{ m s}^{-1}$) that slope down and to the left. Those distinct patterns of the ISWs in the model detach from the slower steady gravity current front. This is clearly seen in the blue colored “wedge” pattern that leans downward and to the left, contoured by the $u = -0.5 \text{ m s}^{-1}$ isoline. Average propagation speeds inferred from the slopes of the -0.3 and -0.5 m s^{-1} isolines in the Hovmöller diagram are -1.53 and -0.48 m s^{-1} for the ISWs and gravity current, respectively (for Run 1, nonlinear propagation speeds are -1.02 and -0.40 m s^{-1} , respectively). Note that, during the time evolution in the model, the solitary waves appear rank ordered, meaning that amplitude and velocity perturbations are stronger for the leading ISW, and subsequently getting weaker for waves generated afterward. This rank order is

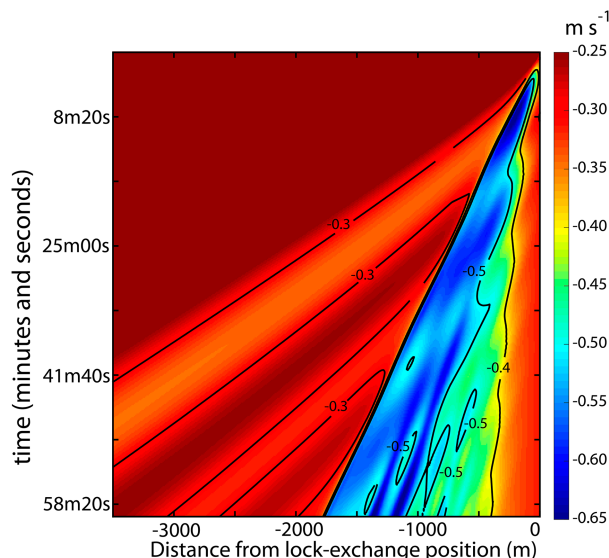


FIG. 11. Hovmöller (space–time) diagram for the surface horizontal velocity. The bright red leftward and downward leaning linear patterns show two consecutive ISWs. The blue colored linear pattern, to the right of the ISWs, shows the gravity current.

observed in most of the satellite images we have analyzed and is consistent with the findings in White and Helfrich (2012) for Type-II regime, i.e., currents that generate upstream undular bores (see also their Fig. 6).

4. Discussion

We found that long-crested ISWs (300 km or more) are visible in Sentinel-3 OLCI true color images owing to strain on sea surface waves exerted by internal wave motions propagating along the main pycnocline of the Pacific Ocean between 5°S and 5°N . Idealized numerical simulations suggest that these ISWs are generated by gravity currents, themselves originating from large-scale fronts associated with TIWs (the NEF and SEF, that bound the equatorial cold tongue). Here, we connect these findings, proposing that these ISWs are upstream-propagating disturbances generated by gravity currents that propagate into the ambient stratification.

a. Gravity current's energy considerations

The propagation of the gravity currents observed in satellite images is subject to energy conservation constraints (WEA, following Simpson 1997). A gravity current, or “density current,” with thickness h and homogeneous density ρ_2 , holds a different potential energy than an adjacent (ambient) water mass with density ρ_1 . The potential energy difference can be written as $\text{PE} = (\rho_1 - \rho_2)g(h/2)$, where g is the acceleration due to gravity. When the system relaxes to equilibrium, assuming complete conversion from potential into kinetic energy $\text{KE} = (1/2)\rho_2 c_0^2$, that is $\text{KE} = \text{PE}$, the gravity current velocity is given by $c_0 = \sqrt{g'h}$, where $g' = g[(\rho_1 - \rho_2)/\rho_2]$ is the reduced gravity.

Based on our model simulation shown in section 3e, itself based on the gravity current measured in November 2008 by WEA, we

estimate h referring to the outcropping $1023.45 \text{ kg m}^{-3}$ isopycnal, at the front. This gives $h = 40 \text{ m}$, in good agreement with $h = 37.9 \text{ m}$ found by WEA. This estimate of h approximates the depth over which horizontal velocities u are homogeneous within representative regions before and after the passage of the gravity current front ($\Delta x \approx \pm 1000 \text{ m}$). The model simulation, averaged from $z = -h$ to $z = 0$, yields densities $\rho_1 = 1023.50 \text{ kg m}^{-3}$ and $\rho_2 = 1023.31 \text{ kg m}^{-3}$ on either side of the gravity current front. In case of complete PE to KE conversion, the resulting front velocity will be $c_0 = -0.27 \text{ m s}^{-1}$, the minus sign indicating leftward motion in Figs. 1c and 10.

However, taking the modeled front velocity u_{f0} , and subtracting the similarly averaged background flow field u_{bk} , yields the actual front velocity u_f in a reference frame moving with the background current:

$$u_f = u_{f0} - u_{\text{bk}}. \quad (2)$$

Using the model, $u_{f0} = -0.48 \text{ m s}^{-1}$ and $u_{\text{bk}} = -0.35 \text{ m s}^{-1}$, the westward speed of the gravity current in the frame of reference of the background flow is $u_f = -0.13 \text{ m s}^{-1}$. The absolute value of u_f is smaller than that of c_0 , as expected, meaning that the energy transfer from PE to KE is not complete. The ratio of the front speed to c_0 may be viewed as a Froude number $\text{Fr}_h = |u_f/c_0| = 0.48$. This value is smaller than that reported by WEA, which is 0.68 for the November 2008 gravity current. WEA pointed out that this value indicates dissipation of energy owing to turbulence, and showed dissipation rates one thousand times greater in the gravity current compared to upstream waters. We further suggest that part of the potential energy is transferred to ISWs generated by the gravity current.

b. Generation mechanism of ISWs

White and Helfrich (2012) showed that gravity currents may transfer energy to upstream propagating ISWs, i.e., ISWs moving ahead of and in the same direction as the gravity current. This is consistent with hydraulic theory and significant to the problem of internal wave generation. These authors demonstrated an analogy with upstream resonance in two-layer flow over variable topography, where gravity currents “act as an obstacle to the flow” and are as effective to generate internal waves upstream as a topographic obstacle. Here we explore the hypothesis that the SSFs and associated gravity currents observed in the study region could generate interfacial waves with some degree of nonlinearity and propagate upstream of the gravity current.

White and Helfrich (2012) used nonlinear hydraulic theory and numerical modeling to classify gravity currents and their upstream flow dynamics. They found a wide range of parameters for which energy exchange between the front and upstream ISWs is significant. This range of parameters was interpreted by these authors as a *transcritical* regime, generating nonlinear internal waves and upstream bores by resonant transfer of energy (see also White and Helfrich 2008). However, ISW generation by gravity currents is more intricate than that by flow over topography since the front is a free

boundary that may interact with the internal waves. The problem is analogous to a dam break setting, in which a volume of fluid with density ρ_2 is released into a two-layer system, where the density and the thickness of the lower layer are, respectively, ρ_0 and d_0 , and the density and thickness of the upper layer are, respectively, ρ_1 and $H - d_0$, where H is total depth. In the model of White and Helfrich (2012), the “lock-exchange” release generates a propagating gravity current with front velocity u_{f0} , and approximate thickness h . (Note that their setting simulates the collapse of denser fluid at the bottom, for comparison with experiments; our model settings are reversed, because we wish to simulate a buoyant gravity current at the surface.) The relative density difference between the gravity current and the ambient water is described by parameter $S \equiv (\rho_0 - \rho_1)/(\rho_0 - \rho_2)$. Defining the reduced gravity as $g^* = g(\rho_0 - \rho_1)/\rho_0$, we have $S = 0.94$ and $g^* = 0.03 \text{ m s}^{-2}$ for our model Run 2. Note that White and Helfrich (2012) scaled all lengths by H , and scaled all velocities by $(g^*H)^{1/2}$. In their model, the linear phase speed in nondimensional units yields then $c_0/\sqrt{g^*H} \approx 0.17$, or an equivalent two-layer system with their parameter $d_0 \approx 0.03$. In our numerical experiment $U = u_{f0}/\sqrt{g^*H} \approx 0.48/10.95 = 0.05$. In the model of White and Helfrich (2012), in the (U, S) parameter plane for $d_0 = 0.1$ (their Fig. 14a), our Run 2 falls into the lower-right corner, for Type II resonant wave generation. Although White and Helfrich (2012) did their classification for gravity currents with lower limit $d_0 = 0.1$, these authors note that the size of the parameter plane that permits internal wave generation upstream of the gravity current front (their Type II class) increases for smaller d_0 and larger S . The case being considered in the equatorial Pacific Ocean, with $d_0 \approx 0.03$, would certainly fall within the Type II class (see White and Helfrich 2012). In this case, internal waves are forced at the front, their amplitude grows, increasing speed through nonlinear dispersion, and consequently are released from the front location when their phase speed exceeds the speed of the propagating front. This sequence is repeated when one solitary wave has completely detached from the front location, which is precisely the result in our numerical simulation (Fig. 10). Therefore, the model results reported in this manuscript are consistent with resonant generation of ISWs, by which energy is transferred from the gravity current to the ISWs. In fact, White and Helfrich (2012) propose that, for ambient parameters similar to our case, as much as 40% of the total energy of the gravity current is used to generate internal waves.

c. ISW spatial structure and age

Concerning the observability of the ISWs in satellite sun glint images (i.e., OLCI true color), we remark that horizontal strain rates at the sea surface typical of internal waves vary from 10^{-4} to 10^{-2} s^{-1} (Mendes et al. 2021; Pinkel 1979). The former value is typical of internal waves generated by river plumes in coastal waters, while the latter is typical for strongly nonlinear ISWs of large amplitude. In fact, fields of surface current divergence/converge at kilometer and subkilometer scales on the order of 10^{-5} s^{-1} have been shown to produce observable contrasts in satellite imagery of the same kind

(Kudryavtsev et al. 2012; see, e.g., their Fig. 6b). The model surface velocity field $u(x)$ for our case study yields a strain rate of about $\partial u/\partial x \approx 2 \times 10^{-4} \text{ s}^{-1}$. This value is similar to that for ISWs observed in the Messina Strait (Mediterranean Sea) which produced strong radar signatures in satellite images (see Alpers and Salusti 1983). ISWs with strain rates of such a magnitude can be detected in sun glint images (Mendes et al. 2021).

As summarized in Fig. 6, in the east Pacific ISWs coexist with sharp fronts all along the equator from the Galapagos Islands (270°E) to the west, up to at least 220°E. Although Fig. 6 only reports an 8-day sequence of surface manifestations of these phenomena, selected owing to particularly good environmental conditions (little cloud cover), we speculate that similar features occurred in all seasons in 2020. Note that for the 8-day period in question, we identify 26 ISW trains, 17 sharp fronts, of which 9 pairs could be clearly related. The age of the ISW trains at the moment of observation may be roughly estimated from the distance between front and leading ISW crest. Assuming an average relative propagation speed of 1 m s^{-1} between ISW and front velocity (the relative speed suggested by the numerical model result), the ISW age is estimated to be between 4 and 55 h. This yields an average age of 28 h for the 9 observed pairs of fronts–ISWs. These values exceed the front’s lifespan from 4 to 11 h estimated by WEA, because ISW energy dissipation is less vigorous than energy dissipation at fronts.

But, as seen in section 3, the SSFs reported by WEA and Yoder et al. (1994) are different from the main thermal signatures north of 1.5°N (west of 262°E) in Fig. 3a, which are larger and broader, and are associated with TIWs and in this case possibly with a TIV. The SSFs are interpreted as buoyant gravity currents, from which ISWs are generated. The distribution of internal wave trains is nearly uniform in latitude. The fewer number of cases found to the north of the equator is due to excessive cloud coverage in the intertropical convergence zone, an area where trade winds converge into a zonal band (Willett et al. 2006). Along the zonal direction, ISWs appear less frequent to the west of 230°E (Fig. 6) where fronts get weaker along the equator.

The ISW phase speeds within the cold tongue are quite variable. We have seen in section 3c that the linear phase speeds may vary by as much as 67% for waves propagating in the zonal direction and 28% for waves propagating in the meridional direction. The above estimates were made for internal wavelengths of 600 m. ISWs that propagate with a prevalent zonal component may propagate slower when they propagate against the EUC, or faster when they propagate in the same direction as the EUC. For the same reason, ISWs may propagate slower when they are generated by gravity currents originating from the TEF, or faster when generated by gravity currents originating from the LEF. We have also seen in section 3d (Fig. 9b) that wavelengths can reach 1500 m, or even higher values. The Taylor–Goldstein equation (1a) is rather sensitive to internal wavelengths, and we next briefly describe phase speed mismatches between the numerical model used in this work, the Taylor–Goldstein equation (1a) for different wavelengths, and observations.

The phase speed derived from Eq. (1a) is based on assuming a wavelength of 600 m, as observed in section 3a, case 2 and on climatological ambient conditions. Rounded to one significant figure, the resulting phase speed is identical to the observation (-0.5 m s^{-1} in both cases). This suggests that the ISWs are in fact characterized by rather small amplitudes that make them behave more or less like linear waves. Otherwise, given the dependency of the phase speed on wave amplitude for ISWs, one would expect the linear phase speed to be significantly smaller than the observed phase speed. It is either this or that the ISWs have indeed large amplitudes but then the climatological ambient conditions do not reflect well the instantaneous conditions.

The mismatch between the observation and the numerical model for the phase speed (-0.5 vs -1.5 m s^{-1} , respectively) and for the wavelength (600 vs 1500 m) is also presumably indicative that the ambient conditions used for model initialization, taken as representative of November 2008, do not represent well the conditions of June 2020 (i.e., case study 2). For example, reducing the depth of the pycnocline from $h_1 = 100 \text{ m}$ to $h_1 = 40 \text{ m}$ (see Table 1 for details) reduces the phase speed from -1.5 to -1.0 m s^{-1} and the wavelength to about 1000 m. Other parameter combinations could well lead to the desired values of observed phase speed and wavelength, but it would require a more systematic numerical study to fully explore the sensitivity of the results to the parameter space. Nevertheless, for the purpose of this observational study, the numerical model used here provides a reasonable physically based ground to propose a general mechanism for the origin of the observed ISWs keeping in mind that the details may not be accurate.

Together with the buoyant gravity currents previously known (WEA; Archer et al. 1997; Johnson 1996; Yoder et al. 1994), which are strongly dissipative, these newly found ISWs may be relevant in the energy budget and turbulent dissipation in the upper equatorial Pacific. As quantified by WEA from shear probes on Chameleon, turbulent dissipation rates of fronts associated with gravity currents were 1000 times greater within the warm and buoyant gravity current layer, compared to that in the cold tongue water underneath. The ISWs reported in this paper may add considerable dissipation into even smaller scales.

d. Broader scope

The existence of the cold tongue in the equatorial Pacific requires a balance between the intense solar heating, the upwelling of cold waters from Ekman divergence near the surface, and the subsurface mixing at the base of the thermocline with colder middle/lower thermocline water. The latter results in cooling of the upper thermocline, and subsequent cooling of surface waters in the cold tongue. While Liu et al. (2016) suggest that many of the mixing events within the cold tongue are caused by lower Richardson numbers resulting from TIWs’ shear instabilities and the EUC, some of the mixing at the upper layer of the thermocline may originate from the deep cycle layer. The “deep cycle” layer is a 24-h cycle of band-limited vertical turbulent motions that extend below the

mixed layer at night. It mixes stratified waters generated by intense solar heating during daytime, together inducing a surface buoyancy flux (see e.g., Moum et al. 2022a,b, 2009). Holmes and Thomas (2015) revealed that TIWs modulate the turbulent heat flux estimated by Moum et al. (2009). Because of such shear driven turbulence, stratification tends to weaken. Vertical mixing within the EUC core is also modulated by TIWs (Moum et al. 2009). The former study reveals that TIW horizontal strain may alter the zonal shear over the EUC core through horizontal vortex stretching, and accounts for some cooling implied in the turbulent heat flux estimated in the latter study. In this paper we add another element to the energy cascade from large to small scales and mixing: the generation of long-crested (typically 300 km) ISWs by relatively long-lived buoyant gravity currents, themselves originating from TIW dynamics (reported by WEA, and references therein). Traveling along the thermocline in the equatorial Pacific cold tongue, these ISWs are subject to strong vertical velocity shears, leading to conditions of “marginal instability” or “marginally stability” (Miles 1961). Consequently, these ISWs may be prone to transient growth instabilities, enhancing mixing in a similar manner as Kelvin–Helmholtz instabilities and wave breaking measured over the continental shelf (Moum et al. 2003). Some of the satellite images analyzed in this study (not shown) are consistent with shorter-scale wave-like features within large ISWs. Passaglia et al. (2018) argue that transient growth instabilities formed in the solitary waves may grow nonlinearly into “optimal disturbance packets.” These packets may in turn generate large Kelvin–Helmholtz instabilities on the forward leaning surface of an ISW that break into turbulence in the rear face of the ISW and downstream of the wave (Carr et al. 2017). All these processes, including the strong dissipation rates associated with the gravity currents measured by WEA, may in the end impact El Niño–Southern Oscillation (ENSO) irregularity and predictability (Holmes et al. 2019; Warner and Moum 2019). The abovementioned measurements, interpretations and our speculations suggest a complex relationship between very different time and space scales. The instabilities’ spatial scales range over at least three orders of magnitude, from TIWs of typically 10^3 km to horizontal scales less than 1 km within ISWs. This relationship would in turn influence coupled ocean–atmosphere phenomena ranging over seasonal and interannual time scales within the equatorial Pacific, possibly with global-scale ramifications.

5. Summary and conclusions

We present a hypothesis for the generation mechanism of trains of ISWs that are observed in the equatorial Pacific Ocean, within a zonal band from 5°S to 5°N; these waves were partly catalogued in a world map of ISWs observed by satellite (Jackson 2007), but to date had not been explained. The presence of these ISWs in this zonal band from 210° to 265°E is remarkable given the absence of steep bottom topography (and tides) that could explain their presence from classical theories (Egbert and Erofeeva 2002). In this study, we provide estimates and model-based predictions of some ISW

characteristics such as their wavelength, crest length, typical amplitude, as well as age. In total, we identified 116 ISW trains during one full year (2020), with an average crest length of 300 km, typical wavelengths of 1500 m, and modeled amplitude of 10 m. The origin of these trains of ISWs is consistent with a generation mechanism that involves buoyant gravity currents with sharp fronts detectable in satellite imagery (visible and thermal infrared from Sentinel-3). The propagation of gravity currents into stably stratified environments is known to generate internal waves (e.g., Nash and Moum 2005; Wang et al. 2019; Bourgault et al. 2016; Mendes et al. 2021), but reports of such phenomena in the open ocean are scarce, if existent at all (WEA; Lavrova and Mityagina 2017). Here we report indications that such an internal wave generation mechanism is ubiquitous along the equatorial Pacific, and we suggest that ISWs may have been overlooked in many other frontal regions in the deep ocean. Energetic TIWs have been linked to buoyant gravity currents in WEA, which propagate within the equatorial cold tongue that is strongly stratified, hence providing conditions for the propagation of ISWs initiated by the gravity currents.

Although ISW generation by gravity currents has previously been simulated for specific conditions (White and Helfrich 2008, 2012), our knowledge of the process is insufficient in open-ocean environments. As such, the use of a numerical model has been helpful for interpreting and complementing the incomplete satellite observations, as well as for making physically based predictions about the properties of the internal wave field. The model appears to simulate the generation of ISWs by resonant interactions under the surface front of the gravity current. The wave amplitude and propagation speed increase through nonlinear dispersion. The wave is subsequently released from the front location when its phase speed significantly exceeds the front speed. If the front propagation is steady (for some period of time at least) the generation sequence is repeated after the complete detachment of the preceding solitary wave. In this process, energy is transferred from the gravity current to ISW trains. The model results are consistent with the satellite observations of internal wave wavelength and phase speed, and the steady propagation of sharp fronts. Energy considerations based on model runs, themselves based on measurements by WEA, show that there is incomplete conversion of potential energy into kinetic energy near the gravity current front. This result is consistent with findings by WEA, which reported that dissipative losses occur owing to turbulence within the gravity current forehead. This potential energy may also transfer to internal waves generated at the front.

Similar ISW trains emanating from sharp fronts were observed in satellite images from 2019 to 2022. While 2019 was an El Niño year, 2020 and 2021 were La Niña years. We expect the surface manifestations of the phenomena reported in this paper to be more visible during La Niña years because thermal fronts are stronger, with a more sharply bound equatorial cold tongue. Perhaps it is no coincidence that the satellite (MODIS) observations reported in Jackson (2007) for the period August 2002–May 2004 (an El Niño period) extend less to the west and are fewer than our own observations

shown in Fig. 2. Furthermore, it is stressed that satellite observations of the sharp fronts and ISWs are compromised during part of the year because of severe cloud cover (typically after September). For that reason, we avoid a seasonal characterization of the ISW features in this study.

The association reported here of sharp ocean fronts and gravity currents with the generation of large-scale ISWs in the open ocean may turn out to be more common than previously thought. New observation techniques with finer resolutions, either by means of remote sensing or field programs, may uncover new insights and quantifications of the cascade of turbulent energy from large to small and smaller scales. For this reason, it is suggested that a comprehensive oceanographic campaign, conducted in the study region, may clarify the issues discussed in this paper. Furthermore, the development of a more complete nonhydrostatic and nonlinear numerical model that could simulate the entire sequence from the large-scale TIWs formation to gravity currents and down to fine-scale ISWs would become an invaluable tool to provide a more comprehensive understanding of these complex interacting phenomena.

Acknowledgments. We are grateful to Christopher Jackson at NOAA for facilitating the use of his global map of internal solitary waves and to three reviewers for their constructive comments. This work was funded by the EU and ESA, under sub-contract CLS-ENV-BC-20-0017 “Multi Sensor Synergy Study for Sentinel-3C/D” between the University of Porto and Collecte Localisation Satellites, SA. A.M.S.-F. gratefully acknowledges FCT and the EU for a Ph.D. grant SFRH/BD/143443/2019. J.C.B.d.S. thanks the Portuguese funding agency Fundação para a Ciência e Tecnologia (FCT) under project IDB/04683/2020.

Data availability statement. The satellite data presented in this study are openly available in Copernicus Open Access Hub: <https://scihub.copernicus.eu/dhus/#/home>, accessed on 9 May 2021. The model data are available on request.

REFERENCES

- Alpers, W., and E. Salusti, 1983: Scylla and Charybdis observed from space. *J. Geophys. Res.*, **88**, 1800–1808, <https://doi.org/10.1029/JC088iC03p01800>.
- Archer, D., and Coauthors, 1997: A meeting place of great ocean currents: Shipboard observations of a convergent front at 2°N in the Pacific. *Deep-Sea Res. II*, **44**, 1827–1849, [https://doi.org/10.1016/S0967-0645\(97\)00031-3](https://doi.org/10.1016/S0967-0645(97)00031-3).
- Behringer, D. W., and Y. Xue, 2004: Evaluation of the global ocean data assimilation system at NCEP: The Pacific Ocean. *Eighth Symp. on Integrated Observing and Assimilation Systems for Atmosphere, Oceans, and Land Surface*, Seattle, WA, Amer. Meteor. Soc., 2.3, https://ams.confex.com/ams/84Annual/techprogram/paper_70720.htm.
- Bourgault, D., and D. E. Kelley, 2004: A laterally averaged non-hydrostatic ocean model. *J. Atmos. Oceanic Technol.*, **21**, 1910–1924, <https://doi.org/10.1175/JTECH-1674.1>.
- , P. Galbraith, and C. Chavanne, 2016: Generation of internal solitary waves by frontally forced intrusions in geophysical flows. *Nat. Commun.*, **7**, 13606, <https://doi.org/10.1038/ncomms13606>.
- Caltabiano, A. C. V., I. S. Robinson, and L. P. Pezzi, 2005: Multi-year satellite observations of instability waves in the tropical Atlantic Ocean. *Ocean Sci.*, **1**, 97–112, <https://doi.org/10.5194/os-1-97-2005>.
- Carr, M., J. Franklin, S. E. King, P. A. Davies, J. Grue, and D. G. Dritschel, 2017: The characteristics of billows generated by internal solitary waves. *J. Fluid Mech.*, **812**, 541–577, <https://doi.org/10.1017/jfm.2016.823>.
- Chin, T. M., J. Vazquez-Cuervo, and E. M. Armstrong, 2017: A multi-scale high-resolution analysis of global sea surface temperature. *Remote Sens. Environ.*, **200**, 154–169, <https://doi.org/10.1016/j.rse.2017.07.029>.
- da Silva, J. C. B., A. L. New, and J. M. Magalhaes, 2011: On the structure and propagation of internal solitary waves generated at the Mascarene Plateau in the Indian Ocean. *Deep-Sea Res. I*, **58**, 229–240, <https://doi.org/10.1016/j.dsr.2010.12.003>.
- Dutrieux, P., C. E. Menkes, J. Vialard, P. Flament, and B. Blanke, 2008: Lagrangian study of tropical instability vortices in the Atlantic. *J. Phys. Oceanogr.*, **38**, 400–417, <https://doi.org/10.1175/2007JPO3763.1>.
- Egbert, G. D., and S. Y. Erofeeva, 2002: Efficient inverse modeling of barotropic ocean tides. *J. Ocean. Atmos. Technol.*, **19**, 183–204, [https://doi.org/10.1175/1520-0426\(2002\)019<0183:EIMOBO>2.0.CO;2](https://doi.org/10.1175/1520-0426(2002)019<0183:EIMOBO>2.0.CO;2).
- Holmes, R. M., and L. N. Thomas, 2015: The modulation of equatorial turbulence by tropical instability waves in a regional ocean model. *J. Phys. Oceanogr.*, **45**, 1155–1173, <https://doi.org/10.1175/JPO-D-14-0209.1>.
- , S. McGregor, A. Santos, and M. H. England, 2019: Contribution of tropical instability waves to ENSO irregularity. *Climate Dyn.*, **52**, 1837–1855, <https://doi.org/10.1007/s00382-018-4217-0>.
- Jackson, C., 2007: Internal wave detection using the Moderate Resolution Imaging Spectroradiometer (MODIS). *J. Geophys. Res.*, **112**, C11012, <https://doi.org/10.1029/2007JC004220>.
- Jackson, C. R., J. C. B. da Silva, and G. Jeans, 2012: The generation of nonlinear internal waves. *Oceanogr.*, **25**, 108–123, <https://doi.org/10.5670/oceanog.2012.46>.
- Johnson, E. S., 1996: A convergent instability wave front in the central tropical Pacific. *Deep-Sea Res. II*, **43**, 753–778, [https://doi.org/10.1016/0967-0645\(96\)00034-3](https://doi.org/10.1016/0967-0645(96)00034-3).
- King, M. D., S. Platnick, W. P. Menzel, S. A. Ackerman, and P. A. Hubanks, 2013: Spatial and temporal distribution of clouds observed by MODIS onboard the Terra and Aqua satellites. *IEEE Trans. Geosci. Remote Sens.*, **51**, 3826–3852, <https://doi.org/10.1109/TGRS.2012.2227333>.
- Kudryavtsev, V., A. Myasoedov, B. Chapron, J. A. Johannessen, and F. Collard, 2012: Imaging mesoscale upper ocean dynamics using synthetic aperture radar and optical data. *J. Geophys. Res.*, **117**, C04029, <https://doi.org/10.1029/2011JC007492>.
- Lavrova, O., and M. Mityagina, 2017: Satellite survey of internal waves in the Black and Caspian Seas. *Remote Sens.*, **9**, 892, <https://doi.org/10.3390/rs9090892>.
- Lian, Q., W. D. Smyth, and Z. Liu, 2020: Numerical computation of instabilities and internal waves from in situ measurements via the viscous Taylor–Goldstein problem. *J. Atmos. Oceanic Technol.*, **37**, 759–776, <https://doi.org/10.1175/JTECH-D-19-0155.1>.
- Liu, C., A. Köhl, Z. Liu, F. Wang, and D. Stammer, 2016: Deep-reaching thermocline mixing in the equatorial Pacific cold

- tongue. *Nat. Commun.*, **7**, 11576, <https://doi.org/10.1038/ncomms11576>.
- Lyman, J. M., G. C. Johnson, and W. S. Kessler, 2007: Distinct 17- and 33-day tropical instability waves in subsurface observations. *J. Phys. Oceanogr.*, **37**, 855–872, <https://doi.org/10.1175/JPO3023.1>.
- Magalhães, J. M., J. C. B. da Silva, M. C. Buijsman, and C. A. E. Garcia, 2016: Effect of the North Equatorial Counter Current on the generation and propagation of internal solitary waves off the Amazon shelf (SAR observations). *Ocean Sci.*, **12**, 243–255, <https://doi.org/10.5194/os-12-243-2016>.
- , W. Alpers, A. M. Santos-Ferreira, and J. C. B. da Silva, 2021: Surface wave breaking caused by internal solitary waves: Effects on radar backscattering measured by SAR and RADAR altimeter. *Oceanography*, **34** (2), 166–176, <https://doi.org/10.5670/oceanog.2021.203>.
- Mendes, R., J. C. B. da Silva, J. M. Magalhaes, B. St-Denis, D. Bourgault, J. Pinto, and J. M. Dias, 2021: On the generation of internal waves by river plumes in subcritical initial conditions. *Sci. Rep.*, **11**, 1963, <https://doi.org/10.1038/s41598-021-81464-5>.
- Miles, J. W., 1961: On the stability of heterogeneous shear flows. *J. Fluid Mech.*, **10**, 496–508, <https://doi.org/10.1017/S0022112061000305>.
- Moum, J. N., D. M. Farmer, W. D. Smyth, L. Armi, and S. Vagle, 2003: Structure and generation of turbulence at interfaces strained by internal solitary waves propagating shoreward over the continental shelf. *J. Phys. Oceanogr.*, **33**, 2093–2112, [https://doi.org/10.1175/1520-0485\(2003\)033<2093:SAGOTA>2.0.CO;2](https://doi.org/10.1175/1520-0485(2003)033<2093:SAGOTA>2.0.CO;2).
- , R. C. Lien, A. Perlin, J. D. Nash, M. C. Gregg, and P. J. Wiles, 2009: Sea surface cooling at the equator by subsurface mixing in tropical instability waves. *Nat. Geosci.*, **2**, 761–765, <https://doi.org/10.1038/ngeo657>.
- , A. Natarov, K. J. Richards, E. L. Shroyer, and W. D. Smyth, 2022a: Mixing in equatorial oceans. *Ocean Mixing: Drivers, Mechanisms and Impacts*, M. Meredith and A. N. Garabato, Eds., Elsevier, 257–273, <https://doi.org/10.1016/B978-0-12-821512-8.00017-7>.
- , and Coauthors, 2022b: Deep cycle turbulence in Atlantic and Pacific cold tongues. *Geophys. Res. Lett.*, **49**, e2021GL097345, <https://doi.org/10.1029/2021GL097345>.
- Nash, J. D., and J. N. Moum, 2005: River plumes as a source of large-amplitude internal waves in the coastal ocean. *Nature*, **437**, 400–403, <https://doi.org/10.1038/nature03936>.
- Osborne, A. R., and T. L. Burch, 1980: Internal solitons in the Andaman Sea. *Science*, **208**, 451–460, <https://doi.org/10.1126/science.208.4443.451>.
- Passaglia, P. Y., K. R. Helfrich, and B. L. White, 2018: Optimal transient growth in thin-interface internal solitary waves. *J. Fluid Mech.*, **840**, 342–378, <https://doi.org/10.1017/jfm.2018.19>.
- Pinkel, R., 1979: Observations of strongly nonlinear internal motion in the open sea using a range-gated Doppler sonar. *J. Phys. Oceanogr.*, **9**, 675–686, [https://doi.org/10.1175/1520-0485\(1979\)009<0675:OOSNIM>2.0.CO;2](https://doi.org/10.1175/1520-0485(1979)009<0675:OOSNIM>2.0.CO;2).
- Santos-Ferreira, A. M., and Coauthors, 2022: Effects of surface wave breaking caused by internal solitary waves in SAR altimeter: Sentinel-3 Copernicus products and advanced new products. *Remote Sens.*, **14**, 587, <https://doi.org/10.3390/rs14030587>.
- Simpson, J. E., 1997: *Gravity Currents: In the Environment and the Laboratory*. 2nd ed. Cambridge University Press, 244 pp.
- Smith, W. H. F., and D. T. Sandwell, 1997: Global sea floor topography from satellite altimetry and ship depth soundings. *Science*, **277**, 1956–1962, <https://doi.org/10.1126/science.277.5334.1956>.
- Smyth, W. D., J. N. Moum, and J. D. Nash, 2011: Narrowband oscillations in the upper equatorial ocean, Part II: Properties of shear instabilities. *J. Phys. Oceanogr.*, **41**, 412–428, <https://doi.org/10.1175/2010JPO4451.1>.
- Stellema, A., A. Sen Gupta, A. Taschetto, and M. Feng, 2022: Pacific equatorial undercurrent: Mean state, sources, and future changes across models. *Front. Climate*, **4**, 933091, <https://doi.org/10.3389/fclim.2022.933091>.
- Tensubam, C. M., N. J. Raju, M. K. Dash, and H. Barskar, 2021: Estimation of internal solitary wave propagation speed in the Andaman Sea using multi-satellite images. *Remote Sens. Environ.*, **252**, 112123, <https://doi.org/10.1016/j.rse.2020.112123>.
- Wang, C., X. Wang, and J. C. B. da Silva, 2019: Studies of internal waves in the Strait of Georgia based on remote sensing images. *Remote Sens.*, **11**, 96, <https://doi.org/10.3390/rs11010096>.
- Warner, S. J., and J. N. Moum, 2019: Feedback of mixing to ENSO phase change. *Geophys. Res. Lett.*, **46**, 13 920–13 927, <https://doi.org/10.1029/2019GL085415>.
- , R. M. Holmes, E. H. M. Hawkins, M. Hoecker-Martínez, A. C. Savage, and J. N. Moum, 2018: Buoyant gravity currents released from tropical instability waves. *J. Phys. Oceanogr.*, **48**, 361–382, <https://doi.org/10.1175/JPO-D-17-0144.1>.
- White, B. L., and K. R. Helfrich, 2008: Gravity currents and internal waves in a stratified fluid. *J. Fluid Mech.*, **616**, 327–356, <https://doi.org/10.1017/S0022112008003984>.
- , and —, 2012: A general description of a gravity current front propagating in a two-layer stratified fluid. *J. Fluid Mech.*, **711**, 545–575, <https://doi.org/10.1017/jfm.2012.409>.
- Willett, C. S., R. R. Leben, and M. F. Lavín, 2006: Eddies and tropical instability waves in the eastern tropical Pacific: A review. *Prog. Oceanogr.*, **69**, 218–238, <https://doi.org/10.1016/j.pocean.2006.03.010>.
- Yoder, J. A., S. G. Ackleson, R. T. Barber, P. Flament, and W. M. Balch, 1994: A line in the sea. *Nature*, **371**, 689–692, <https://doi.org/10.1038/371689a0>.